

Deterministic single-photon source with on-chip 5.6 GHz acoustic clock

Alexander S. Kuznetsov,^{1,*} Meysam Saeedi,¹ Zixuan Wang,^{2,3} Kevin L. Silverman,³ and Klaus Biermann¹

¹*Paul-Drude-Institut für Festkörperelektronik, Leibniz-Institut im*

Forschungsverbund Berlin e.V., Hausvogteiplatz 5-7, 10117 Berlin, Germany

²*Department of Physics, University of Colorado, Boulder, Colorado 80309, USA*

³*National Institute of Standards and Technology, Boulder, Colorado 80305, USA*

(Dated: February 18, 2026)

Scalable solid state single-photon sources (SPSs) with triggered single-photon emission rates exceeding a few GHz would aid in the wide technological adoption of photonic quantum technologies. We demonstrate triggering of a quantum dot (QD) single photon emission using dynamic Purcell effect induced at a frequency of several GHz by acoustic strain. To this end, InAs QDs are integrated in a hybrid photon-phonon patterned microcavity, where the density of optical states is tailored by the lateral confinement of photons in μm -sized traps defined lithographically in the microcavity spacer. The single-photon character of the emission from a QD in a trap is confirmed by measuring single-photon statistics. We demonstrate modulation of the QD transition energy in a trap with a frequency up to 14 GHz by monochromatic longitudinal bulk acoustic phonons generated by piezoelectric transducers. For the modulation frequency of 5.6 GHz, corresponding to the acoustic mode of the microcavity, the QD energy is periodically shifted through a spectrally narrow confined photonic mode leading to an appreciable enhancement of the QD emission due to the dynamic Purcell effect. The platform thus enables the implementation of scalable III-V-based SPSs with on-chip tunable acoustic clocks with frequencies that can exceed several GHz under continuous wave optical excitation.

I. Introduction

Since the first experimental observation of anti-bunching [1], single-photon sources (SPSs) have been identified as a key component of optical quantum technologies [2]. Among a great variety of SPSs, deterministic ones based on semiconductor quantum dots (QDs) [3] arguably have the highest relevance for high performance applications [4].

Under continuous wave optical excitation, solid state QDs can produce single photons with rates up to 80 GHz [5], owing to the shortened radiative lifetimes achieved by photonic engineering. However, the best commercial sources of on-demand SPs are limited to tens-of-MHz rates [6], due to the limited ability to trigger SP emission with rates exceeding a GHz. Such a discrepancy highlights the challenge of realizing practical SPSs that produce on-demand SPs with rates exceeding several GHz.

A well-known strategy towards high-rate SP emission is to combine GHz-rate excitation with high Purcell enhancement of the radiative emission rate. The latter requires placing a QD in a photonic environment with tailored density of optical states such as a nanowire [7], micropillar cavity [8], photonic crystal cavity [9], circular Bragg cavity [10, 11] or an open cavity [12]. In the case of III-V cavities, the Purcell enhancement factor can exceed 20, resulting in the radiative lifetime of III-V QDs down to 30 ps [13, 14], indicating the upper limit of SP rate of about 30 GHz. Moreover, such structures can include contacts for the charge stabilization of QDs [15] or their electrical driving [16, 17]. More conventional approaches to increase the SP triggering rate are based on high-repetition-rate optical pulses produced by electro-optic modula-

tors [18, 19], frequency multiplication [14] and electrical injection [20], and can reach slightly above 1 GHz.

Photonic structures and QDs are sensitive to phonons [21] – static and dynamic strain fields, which can be generated using piezoelectric actuators and transducers, respectively. Static tuning has been successfully applied to demonstrate high Purcell enhancement using strain-tuning by local laser heating [22] and piezo-actuators [23]. In contrast to that, the dynamic strain of surface acoustic waves (SAWs) have been used to modulate the resonance energy of a photonic crystal cavity at 1.6 GHz [24]. The dynamic acoustic strain couples to the excitonic transitions via the deformation potential (DP) mechanism and piezoelectric fields [21] allowing to modulate the transition energies [25], transport excitons [26] as well as coherently control QDs [27–29]. These effects have been used to demonstrate the unconventional triggering of SP emission from bare QDs [30], QDs in photonic crystals [31] and micropillars [32] with sub-GHz frequencies. The fastest acoustic clock reported so far has been demonstrated for bare color centers remotely pumped by a 3.5 GHz SAW [33].

A far less explored approach to realize high-rate SPSs is to trigger the Purcell effect in high quality factor (high-Q) cavities. This dynamic Purcell enhancement relies on the externally triggered, fast crossing between the QD resonance and a photonic mode, as depicted in Fig. 1a. So far, this concept has been demonstrated with 800 MHz SAWs [31] and ps-scale optical pulses with MHz repetition rates [34]. Recently, piezoelectrically generated bulk acoustic waves (BAWs) with frequencies above 5 GHz have been suggested for the Floquet engineering of QDs in microcavities (MCs) [35].

Previously, we have demonstrated that the exciton transition energy of a quantum well embedded in a planar MC can be modulated using piezoelectrically gen-

* corresponding author: kuznetsov@pdi-berlin.de

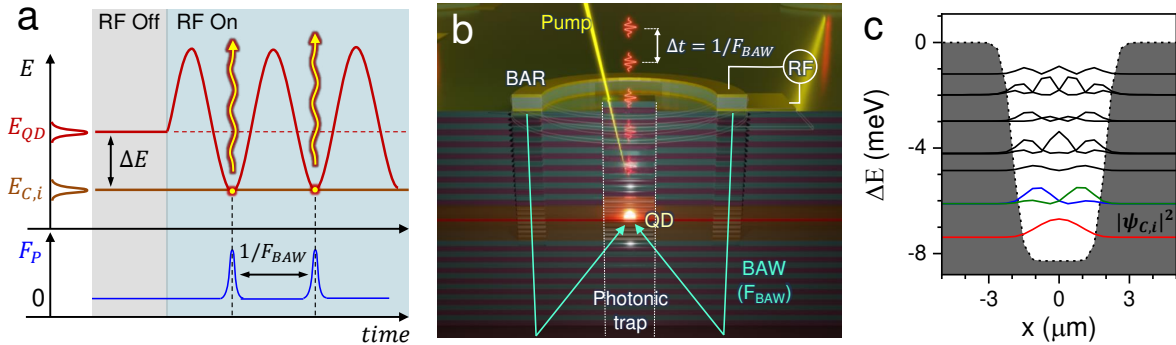


FIG. 1. Dynamic Purcell effect under acoustic modulation. **a** Schematic energy diagram of the system. QD energy is E_{QD} . The energy of an i^{th} confined cavity mode is $E_{C,i}$. The spectral width of the resonances is indicated by Gaussian peaks. Purcell enhancement factor is F_P . The initial cavity-QD detuning (i.e., without the modulation – RF Off) is ΔE . The QD energy is modulated by a BAW, RF On, which results in a periodic resonance with the cavity mode. For simplicity, we assume that the energy modulation amplitude is equal to the static QD-cavity detuning. At resonance there is a large Purcell enhancement leading to the triggered emission of single photons (wiggly lines). **b** A sketch of the MC platform to realize the modulation of panel **a**. An InAs QD is located within a spacer of an AlGaAs MC at the center of a lateral photonic trap, defined by the thicker part of the spacer. A bulk acoustic resonator, BAR, converts an applied radio-frequency signal into a BAW of GHz frequency (F_{BAW}). The BAW propagates towards the center of the trap and modulates the QD via the deformation potential coupling. The device converts a CW pump into a stream of single photons with a rate equal to F_{BAW} . **c** An exemplary calculated spectrum of a $4 \times 4 \mu\text{m}^2$ photonic trap. The dashed line designates the confining potential, defined by the variation of the spacer thickness. The solid lines are spatial profiles of the squared confined wavefunctions.

erated monochromatic longitudinal BAWs [36] at frequencies that reach 20 GHz [37] and very large amplitudes of 50 meV [38]. The large-amplitude energy modulation results in periodic crossings at GHz frequency with multiple spectrally narrow confined optical modes with rates that can reach $dE/dt \sim 1 \text{ meV/ps}$ [39].

In this work, we trigger Purcell enhancement of a cavity-embedded InAs QD emitting single-photons by modulating its transition energy with frequencies up to 14 GHz by BAWs and realizing a dynamical crossing between the QD transition energy and a spectrally narrow confined optical mode at a frequency of 5.6 GHz. The BAWs act as on-chip clock generated by a compact piezoelectric transducer.

II. Results

To realize the dynamic Purcell effect of Fig. 1a, we designed and fabricated a structure, schematically shown in Fig. 1b. The device comprises an AlGaAs MC. Its spacer contains a single layer of InAs self-assembled QDs. The MC details are presented in Methods. It is designed such that the spacer colocalizes (in the growth direction) a 1.3 eV photonic mode and a 6 GHz acoustic phonon. The calculated depth profiles of the optical and acoustic fields are presented in the Supplementary Information SI-Sec.1. The position of the QD layer is chosen to maximize the coupling to the optical and acoustic fields (i.e., close to the anti-nodes of the electric and strain fields). After fabricating the lower DBR and the spacer with QDs, the spacer of the MC is etched producing a few-nm-high and a few- μm -wide mesas. The etching shifts

the cavity mode by approximately 10 meV (SI-Sec.2). The sample is then overgrown with the upper DBR. The mesas act as photonic traps, which create zero-dimensional photonic states. The lateral size and the shape of a trap defines the spectrum of the confined modes, e.g., Fig. 1c. The density of the QDs, which ranges from tens μm^{-2} to $1 \mu\text{m}^{-2}$ and the large number of traps ensure their spatial overlap. Bulk acoustic wave resonators (BARs) are fabricated on the upper DBR around the traps. The active area of a BAR has an aperture for the optical access. As will be discussed later, a monochromatic GHz strain can be injected into the trap by exciting the BAR with a microwave signal.

We first discuss the emission of the traps in the absence of acoustic modulation. The experiments have been carried out at 5 K as described in Methods. Figure 2a shows a spatially and spectrally resolved photoluminescence (PL) map of a $2 \times 2 \mu\text{m}^2$ trap in the high QD density sample region under weak continuous wave non-resonant excitation ($\lambda_{\text{laser}} \approx 804 \text{ nm}$, $P_{\text{laser}} \approx 30 \mu\text{W}$). We identify three emission bands. The band above 1289 meV is a continuum of un-confined states with a large spatial extent. Below 1289 meV there are two modes (designated $E_{C,i}$, where $i = \{0, 1\}$) localized in energy and space, which are the confined modes of the trap. The continuum, corresponds to the parabolic cavity dispersion in the spatially extended etched region, while confined photonic states have flat in-plane momentum (SI-Sec.4). The spatially integrated PL spectrum shown in right side of panel of Fig. 2a, reveals that the emission consists of overlapping narrow peaks, which correspond to different QDs (and possibly to various excitonic complexes). In essence, the confined cavity modes act as a filter for the emission of QDs. From the momentum-resolved (SI-Sec.4) and

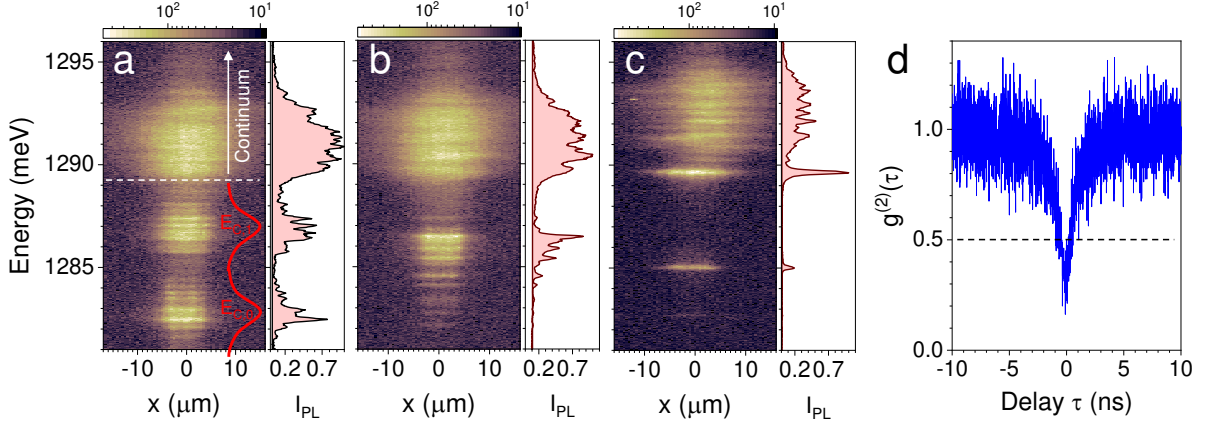


FIG. 2. **Quantum dots in photonic traps.** **a** Spatially and spectrally resolved PL of a $2 \times 2 \mu\text{m}^2$ trap in a high-density of QDs part of the sample under weak non-resonant excitation. The panel on the right is the spatially integrated spectrum. Confined photonic modes are designated $E_{C,0}$ and $E_{C,1}$. **b, c** PL of a $1 \times 1 \mu\text{m}^2$ trap in the high-density and low-density part of the sample, respectively. The excitation conditions are similar to those of panel **a**. The color bars encode the PL intensity in arbitrary units. **d** A second-order auto-correlation measurement as a function of delay ($g^{(2)}(\tau)$) of a single PL peak from a trap in a low-density region.

the excitation power dependent PL measurements (SI-Sec.5), we extract the linewidth and hence the quality factor of both the extended region and the confined modes, which is about $Q = 1500 \pm 100$ and several times smaller than the typical values of 5000–10000 for this type of MCs [40]. The enhanced surface roughness after the overgrowth suggests high photonic disorder of the upper Bragg mirror of the MC.

In the case of a nearby $1 \times 1 \mu\text{m}^2$ trap, there is only one confined mode below the continuum, cf. Fig. 2b. The dependence of the trap spectrum on the lateral trap dimension is presented in SI-Sec.3. Figure 2c presents the PL map of another $1 \times 1 \mu\text{m}^2$ trap located in a region of the sample with low QD density. In striking contrast to the PL of Fig. 2b, only two narrow resonances can be observed below the continuum. This demonstrates that our approach can produce traps with few or single QDs even without post-selection. In order to investigate photon statistics, we measured the second-order auto-correlation function ($g^{(2)}(\tau)$) of a single emission line in a trap. A $g^{(2)}(\tau)$ trace under non-resonant excitation shows a clear dip around $\tau = 0$, cf. Fig. 2d. The $g^{(2)}(0) \approx 0.2$ indicates a clear anti-bunched emission, demonstrating the SP character of PL from a QD in a trap.

We now proceed to discuss the effect of the GHz bulk acoustic wave on the QD emission in the MC. Firstly, we recall that the MC is designed to predominantly couple BAW strain to the QD exciton via the DP mechanism characterized by the coupling strength on the order of 20×10^6 MHz, which is several orders of magnitude larger than the photoelastic coupling [38]. It is this property that allows us to realize the modulation sketched in Fig. 1a.

For the modulation experiment we focused on a $4 \times 4 \mu\text{m}^2$ trap in the low QD density region of the sample, which, unlike the traps discussed above, is located within the aperture of a BAR optimized to excite

a 6 GHz BAW. However, the large generation bandwidth of the BAR allows to generate monochromatic BAWs tunable in the 2–15 GHz range. The electrical characteristic of BARs are presented in SI-Sec.6. Figure 3a shows the dependence of the normalized PL of a QD resonant to a confined optical mode of the trap as a function of the BAW frequency (F_{BAW}) for a fixed BAW amplitude. This time-integrated image clearly shows characteristic signatures of the QD energy modulation, namely, the spectral broadening of the PL line (ΔE). This symmetric broadening corresponds to the harmonic modulation of the QD resonance at F_{BAW} . The largest ΔE values are achieved around 6 GHz, the intended frequency of the MC. Remarkably, the modulation with an amplitude greater than the linewidth is observed up to 14 GHz, limited by the bandwidth of the BAW transducer.

We now turn to the experimental demonstration of the dynamic Purcell effect. Figure 3b shows the dependence of the trap spectrum on the BAW amplitude (A_{BAW}), which is proportional to the microwave (RF) power applied to the transducer, for $F_{\text{BAW}} = 5.6$ GHz. For $A_{\text{BAW}} = 0$, two narrow resonances (designated QD_1 and QD_2) overlap with the photonic ground state ($E_{C,0}$), and a single bright resonance (QD_3) is resonant with $E_{C,1}$. As A_{BAW} is increased, the narrow resonances broaden symmetrically. As is expected for the strain modulation, the maximum ΔE is a linear function of A_{BAW} . Essentially, the modulated QD resonances map out the spectrum of photonic modes.

We observe that the QD_2 energy crosses $E_{C,1}$ for $A_{\text{BAW}} \approx 0.25$, while the QD_3 crosses $E_{C,0}$ for $A_{\text{BAW}} \approx 0.35$. It indicates that the QD_3 resonance is slightly less sensitive to the BAW strain. This could indicate a reduced spatial overlap between the QD position and the phonon mode of the trap. For the largest measured $A_{\text{BAW}} = 0.56$, the maximum ΔE reaches 3 meV. Intensity profiles for QD_2 and QD_3 , taken along the dashed

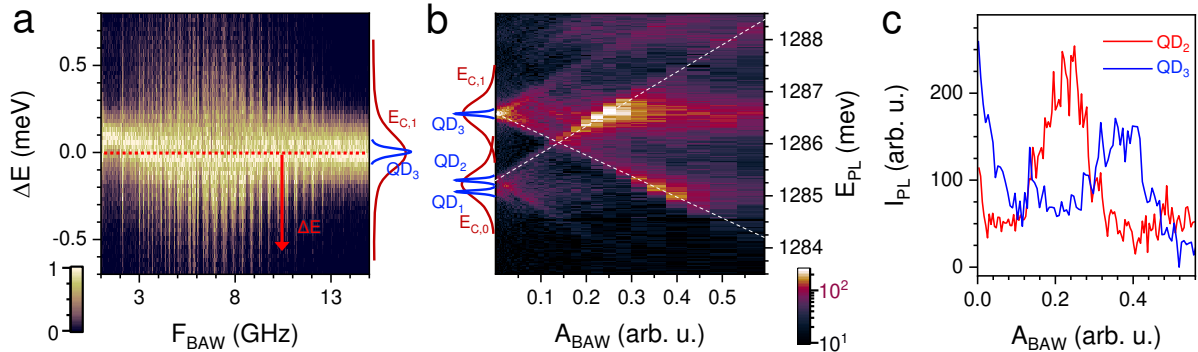


FIG. 3. **GHz acoustic modulation of QDs in photonic traps.** **a** Spectral dependence of a single narrow line resonant to a confined level of a $4 \times 4 \mu\text{m}^2$ trap on BAW frequency (F_{BAW}) for a fixed amplitude ($A_{\text{BAW}} = 0.56$). The energy is referenced to 1286.7 meV. ΔE designates the energy modulation amplitude for a given value of F_{BAW} . For clarity, the spectrum for each frequency was normalized to its maximum. **b** Dependence of the lower confined levels of the same trap on A_{BAW} for $F_{\text{BAW}} = 5.6$ GHz. To improve the QDs energy shifts, the data was filtered using a bandpass filter. The original data and the explanation of the filtering procedure is described in SI-Sec.7. The color bars in panels *a* and *b* encode the PL intensity in arbitrary units. **c** Intensity profiles taken along the dashed lines in the panel *b* for the resonances designated as QD_2 and QD_3 .

lines, are shown in Fig. 3c. For both QDs, the intensity first sharply decreases and then increases during the crossing of the cavity modes. These observations constitute the first demonstration of a dynamic Purcell suppression and enhancement at triggering frequencies exceeding a GHz.

III. Discussion

We have integrated InAs QDs into the spacer of a hybrid photon-phonon patterned AlGaAs MC with μm -sized photonic traps. Small traps were found to contain as few as a single QD in a sample region with low QD density. The SP emission from the QD in a trap was confirmed by measuring the value of $g^{(2)}(0) < 0.5$. We have shown that the dynamical strain of a GHz BAW, piezoelectrically injected into a trap using a BAR, couples to the QD transition energy via the DP mechanism leading to the modification of the QD PL spectrum. Due to the large bandwidth of the BAR, QD spectrum has been harmonically modulated with a frequency up to 14 GHz and considerable energy modulation amplitudes reaching 3 meV and exceeding the energy spacing between confined optical modes. At $F_{\text{BAW}} = 5.6$ GHz, the dynamic crossing between the QD energy and a spectrally narrow confined cavity mode leads to an appreciable enhancement of PL, whereas PL is suppressed when off-resonance, demonstrating the dynamic Purcell suppression and enhancement of SP emission triggered at 5.6 GHz. This work has demonstrated a promising platform for scalable and compact on-demand deterministic SPSs with SP rates that could reach above 10 GHz under continuous wave optical excitation. We highlight that the GHz BAWs act as an on-chip clock for the SP emission.

Based on the literature data for pillar cavities with similar dimensions and Q-factors [41], in our case, a value of Purcell enhancement $F_P \approx 5$ can be rea-

sonably assumed. The typical spontaneous radiative lifetime, i.e., without a cavity, of InAs QDs is $\tau_0 \approx 850$ ps [13]. Hence, we estimate the Purcell-shortened lifetime $\tau = \tau_0/F_P = 170$ ps, which corresponds to the rate $1/\tau \approx 5.9$ GHz. This demonstrates the potential to trigger single-photon generation at GHz frequencies using on-chip acoustic devices.

We note that similar MCs with quantum wells typically have $Q \approx 7500$, while in the present case $Q \approx 1500 \pm 100$. This discrepancy is most likely due to the MBE overgrowth parameters (e.g., substrate temperature and surface cleaning before the overgrowth) being not optimized for the new type of sample. Beyond improving the Q factor, the next generation of the MC would include doped layers for the charge stabilization [42], which would enable $g^{(2)}(\tau)$ measurements under resonant optical excitation. Furthermore, a natural next step is to deterministically fabricate photonic traps around QDs using in-situ lithography assisted by optical mapping [43]. The BAW frequency could be pushed to 20 GHz by reducing the BAR piezoelectric film thickness or using high acoustic velocity piezoelectrics (e.g., AlScN). Piezoelectric transducers generating at frequencies exceeding 50 GHz have recently been demonstrated [44].

We point out another interesting aspect of our platform. As can be seen in Fig. 3b, for $A_{\text{BAW}} > 0.35$, the QD_2 energy shifts above $E_{C,1}$, which means that it passes $E_{C,1}$ two times per cycle effectively doubling the emission rate. Furthermore, the energy modulation rate, $v_{\text{Mod}} = dE/dt$, determines the time-jitter of the SP emission ($d\tau_{\text{SP}}$). For the maximum realized energy shift of the QD_2 of $\Delta E = 3$ meV, cf. Fig. 3b, we obtain $v_{\text{Mod}} \approx 2\Delta E/T_{\text{BAW}} * (f_E/f_T) = 0.1$ meV/ps, where $T_{\text{BAW}} = 1/F_{\text{BAW}} = 178$ ps, $f_E \approx 0.68$ is the fraction of the peak-to-peak energy shift, which is quasi-linear for the sinusoidal modulation, and $f_T \approx 0.22$ is the corresponding fraction of the modulation period. Hence, $d\tau_{\text{SP}} \approx dE_{C,1}/v_{\text{Mod}} \approx 9$ ps, where $dE_{C,1} \approx 0.9$ meV

is the energy full width at half maximum of the confined mode of the trap. The time-jitter can be decreased by increasing either the modulation frequency or its amplitude, and decreasing the linewidth by employing higher-Q MCs.

Finally, we note another unique aspect of our platform. Due to dynamic crossing of a QD with multiple optical modes, continuous wave optical excitation can be resonant with one mode, while SP emission can be detected from a mode below or above. This excitation scheme could completely eliminate the contamination due to the laser photons. Due to the large photon-QD-phonon coupling rates, the platform is also attractive for the quantum transduction between the microwave and optical domains.

Methods

QD microcavity sample

The basic design of the MC has been detailed in Refs. [39, 40]. In short, here we rely on the “double magic coincidence” [45, 46] exhibited in (Al,Ga)As systems between light and GHz acoustic vibrations. The latter means that the spacer of the MC co-localizes optical fields of approximately 300 THz and longitudinal acoustic strain in the GHz range. The planar MC is expected to have $Q = 5000$. The spacer of the MC contains a single layer of self-assembled InAs QDs emitting single photons in the 900–950 nm range. The whole MC structure is designed such that QDs are located very close to both photon and phonon anti-nodes. The strain predominantly couples to QDs via the DP mechanism [37].

First, the molecular beam epitaxy (MBE) is used to grow the lower DBR and the cavity spacer with QDs. The spacer is then subjected to shallow etching (etching depth of approx. 10 nm) with micrometer lateral scale. Etching takes place at least 200 nm away from the QD depth. The sample is then re-inserted into the MBE chamber and the upper DBR is overgrown. The patterning leads to the lateral confinement of the photonic mode. No post-selection of QDs is done.

Bulk acoustic wave transducers

The acoustic mode at $F_M \approx 5.6$ GHz of the MC was resonantly driven by a BAR [36] fabricated on top of the region containing the trap and excited using an RF generator, cf. Fig. 1a. The longitudinal BAW is excited via the piezoelectric effect by the BAR away from the trap. The BAW reaches the center of the trap after lat-

eral propagation involving multiple reflections between the polished bottom and top sides of the sample. The amplitude of the BAW can be precisely controlled by the RF power applied to BAR. A signal-ground RF probe was used to connect the bottom and top electrodes of the transducer to an RF generator with high-power output (up to 25 dBm).

Optical measurements under modulation

Optical measurements under acoustic excitation were carried out in a cold-finger liquid-He cryogenic probe station at 5 K temperature. BARs were electrically contacted using RF probes. A single-mode continuous wave external cavity-stabilized Ti-Sapphire laser was used to non-resonantly excite QDs for PL measurements with BAW modulation. The laser was focused on the sample at normal incidence using a 10x objective resulting in a few- μm Gaussian-like spot positioned on the trap. PL measurements integrated over 0.1–1 second with moderate spectral resolution of 0.1 meV, were carried out by transferring PL image of the trap on the entrance slit of a single grating spectrometer and recorded using a nitrogen-cooled CCD camera.

The second-order autocorrelation measurements $g^{(2)}(\tau)$ are performed using a setup similar to that described in Ref. [28]. The sample is mounted in a closed-cycle cryostat and cooled to approximately 5 K. Excitation is provided by a 640 nm laser focused onto the sample through a microscope objective with a numerical aperture of 0.81. The reflected laser light is separated from the PL signal using an 850 nm long-pass filter. A single emission line is then spectrally isolated with a narrow band-pass filter of about 2 nm bandwidth. The filtered PL is directed to a 50:50 non-polarizing beamsplitter, and the two output ports are coupled to superconducting nanowire single-photon detectors. Photon arrival times from the two detectors are recorded by a picosecond-resolution event timer, and the coincidence histogram is constructed using standard time-correlated single-photon counting techniques to obtain $g^{(2)}(\tau)$.

Data availability

The measurement and numerical simulation data that support the findings within this study are included within the main text and Supplementary Information and can also be made available upon request from the corresponding author.

-
- [1] H. J. Kimble, M. Dagenais, and L. Mandel, Photon antibunching in resonance fluorescence, *Phys. Rev. Lett.* **39**, 691 (1977).
 [2] P. Senellart, G. Solomon, and A. White, High-performance semiconductor quantum-dot single-photon sources, *Nat. Nanotechnol.* **12**, 1026 (2017).

- [3] P. Michler, A. Kiraz, C. Becher, W. V. Schoenfeld, P. M. Petroff, L. Zhang, E. Hu, and A. Imamoglu, A quantum dot single-photon turnstile device, *Science* **290**, 2282 (2000).
 [4] G. Liu, W. Zhou, D. Gromyko, D. Huang, Z. Dong, R. Liu, J. Zhu, J. Liu, C. W. Qiu, and L. Wu, Single-photon generation and manipulation in quantum

- nanophotonics, *Appl. Phys. Rev.* **12**, 011308 (2025).
- [5] T. B. Hoang, G. M. Akselrod, and M. H. Mikkelsen, Ultrafast Room-Temperature Single Photon Emission from Quantum Dots Coupled to Plasmonic Nanocavities, *Nano Lett.* **16**, 270 (2016).
 - [6] H. Georgieva, P. Stepanov, L. Sewidan, A. Pishchagin, M. López, and S. Kück, Metrological characterization of a commercial single-photon source with high photon flux emission, *Metrologia* **61**, 054001 (2024).
 - [7] J. Claudon, J. Bleuse, N. S. Malik, M. Bazin, P. Jaffrennou, N. Gregersen, C. Sauvan, P. Lalanne, and J. M. Gérard, A highly efficient single-photon source based on a quantum dot in a photonic nanowire, *Nat. Photonics* **4**, 174 (2010).
 - [8] O. Gazzano, S. Michaelis De Vasconcellos, C. Arnold, A. Nowak, E. Galopin, I. Sagnes, L. Lanco, A. Lemaître, and P. Senellart, Bright solid-state sources of indistinguishable single photons, *Nat. Commun.* **4**, 1425 (2013).
 - [9] K. H. Madsen, S. Ates, J. Liu, A. Javadi, S. M. Albrecht, I. Yeo, S. Stobbe, and P. Lodahl, Efficient out-coupling of high-purity single photons from a coherent quantum dot in a photonic-crystal cavity, *Phys. Rev. B* **90**, 155303 (2014).
 - [10] L. Sapienza, M. Davanço, A. Badolato, and K. Srinivasan, Nanoscale optical positioning of single quantum dots for bright and pure single-photon emission, *Nat. Commun.* **6**, 7833 (2015).
 - [11] H. Abudayyeh, A. Mildner, D. Liran, B. Lubotzky, L. Lüder, M. Fleischer, and R. Rapaport, Overcoming the Rate-Directionality Trade-off: A Room-Temperature Ultrabright Quantum Light Source, *ACS Nano* **15**, 17384 (2021).
 - [12] N. Tomm, A. Javadi, N. O. Antoniadis, D. Najer, M. C. Löbl, A. R. Korsch, R. Schott, S. R. Valentin, A. D. Wieck, A. Ludwig, and R. J. Warburton, A bright and fast source of coherent single photons, *Nat. Nanotechnol.* **16**, 399 (2021).
 - [13] A. Chellu, S. Bej, H. Wahl, H. Kahle, T. Uusitalo, R. Hytönen, H. Rekola, J. Lång, E. Schöll, L. Hanschke, P. Kallert, T. Kipp, C. Stelow, M. Tuominen, K. D. Jöns, P. Karvinen, T. Niemi, M. Guina, and T. Hakkarainen, Purcell-enhanced single-photon emission from InAs/GaAs quantum dots coupled to broadband cylindrical nanocavities, *ArXiv* (2024), [arXiv:2407.11642v2](https://arxiv.org/abs/2407.11642v2).
 - [14] L. Rickert, D. A. Vajner, M. von Helversen, J. Schall, S. Rodt, S. Reitzenstein, H. Liu, S. Li, H. Ni, Z. Niu, and T. Heindel, High Purcell Enhancement in Quantum-Dot Hybrid Circular Bragg Grating Cavities for GHz Clock Rate Generation of Indistinguishable Photons, *ACS Photonics* **12**, 464 (2025).
 - [15] N. Somaschi, V. Giesz, L. De Santis, J. C. Loredano, M. P. Almeida, G. Hornecker, S. L. Portalupi, T. Grange, C. Antón, J. Demory, C. Gómez, I. Sagnes, N. D. Lanzillotti-Kimura, A. Lemaître, A. Auffeves, A. G. White, L. Lanco, and P. Senellart, Near-optimal single-photon sources in the solid state, *Nat. Photonics* **10**, 340 (2016).
 - [16] T. Heindel, C. Schneider, M. Lermer, S. H. Kwon, T. Braun, S. Reitzenstein, S. Höfling, M. Kamp, and A. Forchel, Electrically driven quantum dot-micropillar single photon source with 34% overall efficiency, *Appl. Phys. Lett.* **96**, 011107 (2010).
 - [17] W. Unrau, D. Quandt, J. H. Schulze, T. Heindel, T. D. Germann, O. Hitzemann, A. Strittmatter, S. Reitzenstein, U. W. Pohl, and D. Bimberg, Electrically driven single photon source based on a site-controlled quantum dot with self-aligned current injection, *Appl. Phys. Lett.* **101**, 211119 (2012).
 - [18] M. Anderson, T. Müller, J. Skiba-Szymanska, A. B. Krysa, J. Huwer, R. M. Stevenson, J. Heffernan, D. A. Ritchie, and A. J. Shields, Gigahertz-Clocked Teleportation of Time-Bin Qubits with a Quantum Dot in the Telecommunication C Band, *Phys. Rev. Appl.* **13**, 054052 (2020).
 - [19] M. Poortvliet, P. Steindl, I. Kuijff, H. Visser, A. Van Amersfoort, and W. Löffler, Picosecond laser pulses for quantum dot-microcavity-based single-photon generation by cascaded electro-optic modulation of a narrowlinewidth laser, *Phys. Rev. Appl.* **23**, 014017 (2025).
 - [20] Y. Lin, Y. Ye, and W. Fang, Electrically driven single-photon sources, *J. Semicond.* **40**, 071904 (2019).
 - [21] M. M. De Lima and P. V. Santos, Modulation of photonic structures by surface acoustic waves, *Reports Prog. Phys.* **68**, 1639 (2005).
 - [22] P. Mudi, C.-W. Shih, M. Holzer, M. Elhajhasan, I. Limame, I. Hüllen, C. C. Palekar, S. Banerjee, A. Koulas-Simos, K. Gaur, V. Deshpande, C. Dubourdieu, G. Callsen, and S. Reitzenstein, Laser-induced spectral tuning of single quantum dots embedded into microposts clad with HfO₂, *Appl. Phys. Lett.* **125**, 053502 (2024).
 - [23] J. Yang, Y. Chen, Z. Rao, Z. Zheng, C. Song, Y. Chen, K. Xiong, P. Chen, C. Zhang, W. Wu, Y. Yu, and S. Yu, Tunable quantum dots in monolithic Fabry-Perot microcavities for high-performance single-photon sources, *Light Sci. Appl.* **13**, 0 (2024).
 - [24] D. A. Fuhrmann, S. M. Thon, H. Kim, D. Bouwmeester, P. M. Petroff, A. Wixforth, and H. J. Krenner, Dynamic modulation of photonic crystal nanocavities using gigahertz acoustic phonons, *Nat. Photonics* **5**, 605 (2011).
 - [25] A. V. Akimov, A. V. Scherbakov, D. R. Yakovlev, C. T. Foxon, and M. Bayer, Ultrafast band-gap shift induced by a strain pulse in semiconductor heterostructures, *Phys. Rev. Lett.* **97**, 037401 (2006).
 - [26] S. Lazić, P. Santos, and R. Hey, Exciton transport by moving strain dots in GaAs quantum wells, *Phys. E Low-dimensional Syst. Nanostructures* **42**, 2640 (2010).
 - [27] D. D. Bühler, M. Weiß, A. Crespo-Poveda, E. D. Nysten, J. J. Finley, K. Müller, P. V. Santos, M. M. de Lima, and H. J. Krenner, On-chip generation and dynamic piezo-optomechanical rotation of single photons, *Nat. Commun.* **13**, 6998 (2022).
 - [28] R. A. DeCrescent, Z. Wang, J. T. Bush, P. Imany, A. Kwiatkowski, D. V. Reddy, S. W. Nam, R. P. Mirin, and K. L. Silverman, Coherent dynamics in an optical quantum dot with phonons and photons, *Optica* **11**, 1526 (2024).
 - [29] Y. Zhan, Z. Wang, R. P. Mirin, K. L. Silverman, and S. Sun, Dynamical Acoustic Control of Resonance Fluorescence from a Strongly Driven Two-Level System, *ArXiv* (2025), [arXiv:2509.25847v1](https://arxiv.org/abs/2509.25847v1).
 - [30] O. D. D. Couto, S. Lazić, F. Iikawa, J. A. H. Stotz, U. Jahn, R. Hey, and P. V. Santos, Photon anti-bunching in acoustically pumped quantum dots, *Nat. Photonics* **3**, 645 (2009).
 - [31] M. Weiß, S. Kapfinger, T. Reichert, J. J. Finley, A. Wixforth, M. Kaniber, and H. J. Krenner, Surface acoustic wave regulated single photon emission from a coupled quantum dot-nanocavity system, *Appl. Phys. Lett.* **109**, 033105 (2016).

- [32] B. Villa, A. J. Bennett, D. J. Ellis, J. P. Lee, J. Skiba-Szymanska, T. A. Mitchell, J. P. Griffiths, I. Farrer, D. A. Ritchie, C. J. Ford, and A. J. Shields, Surface acoustic wave modulation of a coherently driven quantum dot in a pillar microcavity, *Appl. Phys. Lett.* **111**, 011103 (2017).
- [33] M. Yuan, K. Biermann, S. Takada, C. Bäuerle, and P. V. Santos, Remotely Pumped GHz Antibunched Emission from Single Exciton Centers in GaAs, *ACS Photonics* **8**, 758 (2021).
- [34] E. Peinke, T. Sattler, G. M. Torelly, P. L. Souza, S. Perret, J. Bleuse, J. Claudon, W. L. Vos, and J. M. Gérard, Tailoring the properties of quantum dot-micropillars by ultrafast optical injection of free charge carriers, *Light Sci. Appl.* **10**, 215 (2021).
- [35] D. Groll, D. Wigger, M. Weiß, M. Yuan, A. Kuznetsov, A. Hernández-Mínguez, H. J. Krenner, T. Kuhn, and P. Machnikowski, Acousto-optical Floquet engineering of a single-photon emitter, *ArXiv* (2025), [arXiv:2509.09559](https://arxiv.org/abs/2509.09559).
- [36] D. H. O. Machado, A. Crespo-Poveda, A. S. Kuznetsov, K. Biermann, L. V. A. Scalvi, and P. V. Santos, Generation and propagation of super-high-frequency bulk acoustic wave in GaAs, *Phys. Rev. Appl.* **12**, 1 (2019).
- [37] A. S. Kuznetsov, D. H. O. Machado, K. Biermann, and P. V. Santos, Electrically Driven Microcavity Exciton-Polariton Optomechanics at 20 GHz, *Phys. Rev. X* **11**, 021020 (2021).
- [38] P. Sesin, A. S. Kuznetsov, G. Rozas, S. Anguiano, A. E. Bruchhausen, A. Lemaître, K. Biermann, P. V. Santos, and A. Fainstein, Giant optomechanical coupling and dephasing protection with cavity exciton-polaritons, *Phys. Rev. Res.* **5**, L042035 (2023).
- [39] A. Kuznetsov, I. Carraro-Haddad, G. Usaj, K. Biermann, A. Fainstein, and P. V. Santos, Ground state exciton-polariton condensation by coherent Floquet driving, *ArXiv* (2025), [arXiv:2506.05874](https://arxiv.org/abs/2506.05874).
- [40] A. S. Kuznetsov, K. Biermann, A. A. Reynoso, A. Fainstein, and P. V. Santos, Microcavity phonoritons – a coherent optical-to-microwave interface, *Nat. Commun.* **14**, 5470 (2023).
- [41] A. Dousse, L. Lanco, J. Suffczyński, E. Semenova, A. Miard, A. Lemaître, I. Sagnes, C. Roblin, J. Bloch, and P. Senellart, Controlled light-matter coupling for a single quantum dot embedded in a pillar microcavity using far-field optical lithography, *Phys. Rev. Lett.* **101**, 267404 (2008).
- [42] Z. Wang, R. A. DeCrescent, P. Imany, J. T. Bush, D. V. Reddy, S. Woo Nam, R. P. Mirin, and K. L. Silverman, Gated InAs quantum dots embedded in surface acoustic wave cavities for low-noise optomechanics, *Opt. Express* **32**, 38384 (2024).
- [43] S. Rodt and S. Reitzenstein, High-performance deterministic in situ electron-beam lithography enabled by cathodoluminescence spectroscopy, *Nano Express* **2**, 014007 (2021).
- [44] J. Kramer, B. T. Bosworth, L. Matto, N. R. Jungwirth, O. Barrera, F. Bergmann, S. Cho, V. Chulukhadze, M. Goorsky, N. D. Orloff, and R. Lu, Acoustic resonators above 100 GHz, *Appl. Phys. Lett.* **127**, 012204 (2025).
- [45] M. Trigo, A. Bruchhausen, A. Fainstein, B. Jusserand, and V. Thierry-Mieg, Confinement of acoustical vibrations in a semiconductor planar phonon cavity, *Phys. Rev. Lett.* **89**, 227402 (2002).
- [46] A. Fainstein, N. D. Lanzillotti-Kimura, B. Jusserand, and B. Perrin, Strong optical-mechanical coupling in a vertical GaAs/AlAs microcavity for subterahertz phonons and near-infrared light, *Phys. Rev. Lett.* **110**, 037403 (2013).

Acknowledgments

A.S.K. acknowledges the funding from DFG grant 359162958. We are grateful to Dr. Kevin L. Silverman for the expert knowledge on QDs. The authors thank Dr. Valentino Pistore for a critical review of the manuscript.

Author contributions

A.S.K. performed the spectroscopic experiments with acoustic modulation and carried out the respective analysis. M.S. fabricated bulk acoustic transducers. Z.W. carried out the photon correlation measurements. Sample design was done by K.B. with the input of all authors. K.L.S. fabricated the lower half of the MC with QDs. K.B. performed the MBE overgrowth of the samples. A.S.K. has conceived the idea and written the manuscript with the input from all authors.

Competing interests

The authors declare no competing interests.

Supplementary Information:
Deterministic single-photon source with on-chip 5.6 GHz acoustic clock

Alexander S. Kuznetsov,^{1,*} Meysam Saeedi,¹ Zixuan Wang,^{2,3} Kevin L. Silverman,³ and Klaus Biermann¹

¹*Paul-Drude-Institut für Festkörperelektronik, Leibniz-Institut in*

Forschungsverbund Berlin e.V., Hausvogteiplatz 5-7, 10117 Berlin, Germany

²*Department of Physics, University of Colorado, Boulder, Colorado 80309, USA*

³*National Institute of Standards and Technology, Boulder, Colorado 80305, USA*

This document contains additional material to support the conclusions of the main text.

* corresponding author: kuznetsov@pdi-berlin.de

1. Microcavity optical and acoustic properties

The microcavity (MC) design is based on the one in Ref. [1], where we studied acoustic modulation of light-matter exciton-polaritons. We take advantage of the optical and acoustic coincidence of AlGaAs [2], where an AlGaAs MC designed for photons in the 800–900 nm range acts as a MC for GHz longitudinal bulk acoustic phonons. The MC consists of a spacer, which contains a delta-like layer of InAs self-assembled quantum dots (QDs), sandwiched between a lower (LDBR) and an upper (UDBR) distributed Bragg reflectors (DBRs). Each DBR period consists of a stack of three pairs of $\text{Al}_{x_1}\text{Ga}_{(1-x_1)}\text{As}/\text{Al}_{x_2}\text{Ga}_{(1-x_2)}\text{As}$ layers, each with an optical thickness $\lambda/4$. The thicknesses d_1 and d_2 and Al compositions x_1 and x_2 of the layers pairs are listed in Table I.

TABLE I: Layer structure of the MC sample. The DBRs consist of stacks of $\text{Al}_{x_1}\text{Ga}_{1-x_1}\text{As}$ and $\text{Al}_{x_2}\text{Ga}_{1-x_2}\text{As}$ layers with thicknesses d_1 and d_2 and Al compositions x_1 and x_2 , respectively. d_T and n_{rep} are, respectively, the total thickness and the number of repetition periods.

Region	d_T (nm)	n_{rep}	$d_1 : d_2$ (nm)	$x_1 : x_2$	Comment				
UDBR	4978.6	11	76.9:69.5	0.6:0.05	pair ₃				
			81.2:69.5	0.95:0.05	pair ₂				
			81.2:74.3	0.95:0.4	pair ₁				
spacer	69.5	1	69.5	0.05	growth interruption				
						—	—	—	
						197.9	1	197.9	0.05
						10	1	10	0
						***	***	***	***
10	1	10	0						
129.3	1	129.3	0.05						
LDBR	6336.4	14	76.9:69.5	0.6:0.05	pair ₃				
			81.2:69.5	0.95:0.05	pair ₂				
			81.2:74.3	0.95:0.4	pair ₁				
substrate					GaAs(001) S-I substrate (double side polished)				

Figure SI 1a shows the depth profiles of the refractive index and the normalized acoustic impedance of a region around the MC spacer. These curves show that the layers will act in a similar manner on both a ~ 950 nm photon and a few GHz acoustic phonon modes. Curves of Figs. SI 1b,c depict the depth profiles of the optical and acoustic fields calculated using a transfer matrix approach. The spacer layer acts as a $3/2\lambda_{\text{photon}}$ optical and λ_{phonon} acoustic cavity. When designing the MC, we make sure that the QD layer is positioned close to both optical and acoustic field anti-nodes. This design maximizes the deformation potential coupling of the acoustic strain to the QD excitons, which dominates over any photoelastic coupling [3].

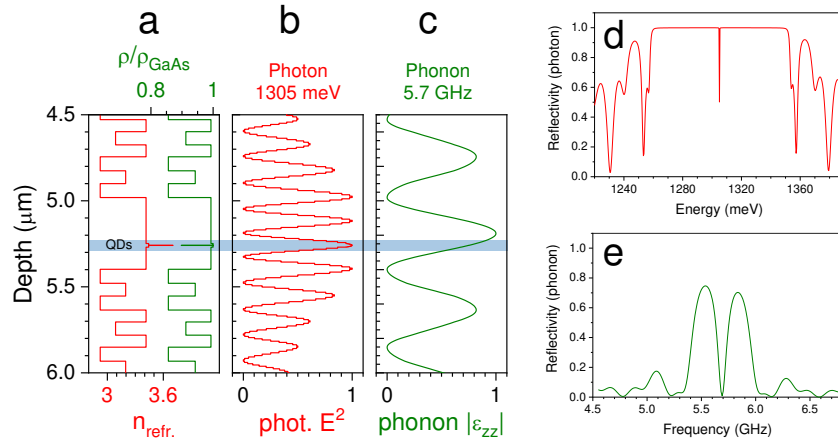


Fig. SI 1: **Simulated microcavity optical and acoustic responses.** **a** Depth profiles of the refractive index and normalized mass density, **b** optical field at 1305 meV and **c** amplitude of 5.6 GHz phonon strain around the MC spacer (zero at the surface). **d,e** Calculated optical and acoustic reflectivity spectra, respectively.

Figures SI 1d,e show simulated optical and acoustic reflectivities, respectively. Both plots exhibit clear stopband regions with well-defined cavity modes at 950 nm (photons) and 5.7 GHz (phonons). Due to the lower number of acoustic DBR pairs, the acoustic cavity resonance is broad, which translates in an acoustic quality factor of $Q_a \approx 300$, while the optical one is $Q_o \approx 5000$.

2. Spatial reflectivity

Here we discuss spatial dependence of MC reflectivity. The studied microcavity was grown on a quarter of a 3" GaAs wafer as schematically shown in Figures SI 2a. There, the dashed red line shows the spatial direction of the reflectivity scan. Reflectivity of the non-etched and etched regions have been measured on a structure that is schematically shown in Figures SI 2b. It consists of a $160 \times 120 \mu\text{m}^2$ non-etched (nER) mesa surrounded by etched (ER) area. The large areas of the nER and ER ensure that no lateral confinement of photonic modes is present.

Figures SI 2c,d show spatial reflectivity of non-etched and etched areas, respectively measured at 5 K. Both maps show very clear parabolic spatial dispersion of the optical resonances, characteristic of the MBE growth under rotation.

Figure SI 2e depicts exemplary nER and ER curves for a fixed measurement position. In both curves, a flat region in the reflectivity corresponds to an optical stopband. In the stopband, there is a single narrow resonance due to the optical mode. A zoom-in of the optical mode, cf. Figure SI 2f, shows that the ER resonance is blueshifted by approximately 10 meV with respect to the one in the nER, which is the consequence of the etching of the MC spacer. The magnitude of the energy shift directly translates to the depth of the confinement potential as will be discussed in the next section.

We note that the linewidth of the optical resonances is artificially broadened due to the numerical aperture of the 10x objective used in the measurement. The weak signature of the ER optical mode in the ER spectrum is due to the fact that the reflectivity sampling area is larger than the size of the nER region.

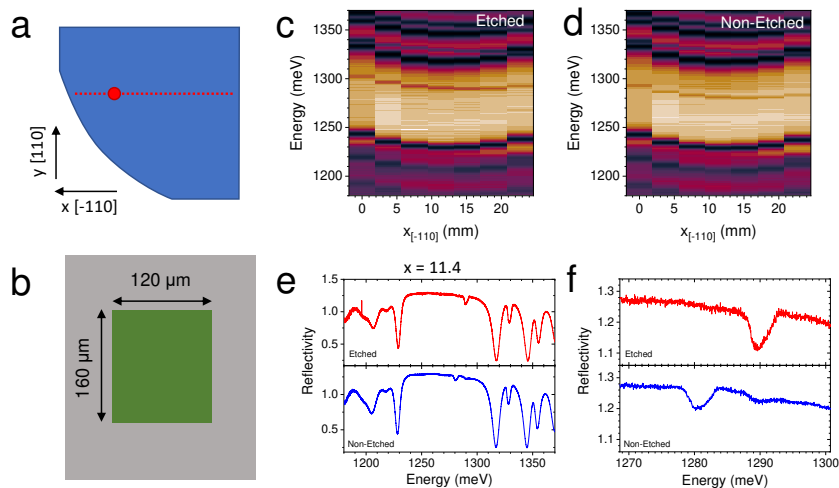


Fig. SI 2: **Spatial optical reflectivity.** **a** A sketch of the microcavity sample. The red dot corresponds to the $x = 0$ mm position. **b** A sketch of the area used to measure the reflectivity of the non-etched (green rectangle) and etched (gray shaded area) regions. **c,d** Reflectivity spectra of spatially extended etched and non-etched MC regions measured across the sample at 5 K. The zero value corresponds to the red point in **a**. The bright colors correspond to higher reflectivity. **e** Single spectra of the etched and non-etched regions at $x = 11$ mm. The values of the reflectivity larger than unit are an artifact of normalization to the reflectivity reference. **f** Zoom of the spectra in **c** in the range of the cavity modes.

3. Photonic confinement

The lateral zero-dimensional photonic confinement is introduced by creating micron-scale lateral mesas in the spacer of the microcavity by shallow (approx. 10 nm) etching followed by the MBE overgrowth [4]. As was discussed in the previous section, such etching introduces up to 10 meV energy shifts between the cavity resonances in the etched and non-etched regions. The size and the shape of the mesa, which acts as a trap, then dictates the structure of the confined levels.

Figure SI 3a shows an exemplary atomic force microscope image of a $5 \times 5 \mu\text{m}^2$ trap after the overgrowth. Optical lithography enables the fabrication of traps with lateral dimension (L) down to $L = 1 \mu\text{m}$. We have investigated confinement in traps with $L = 10 \mu\text{m}$ down to $L = 1 \mu\text{m}$, cf. Figure SI 3b.

Figures SI 3c,d depict spectrally and spatially resolved photoluminescence (PL) maps of $L = 10 \mu\text{m}$ and $L = 2 \mu\text{m}$ traps under weak non-resonant optical excitation at 5 K. As discussed in the main text, above approximately 1290 meV, the emission arises from the spatially extended continuum of states from the barrier (which is the spatially extended etched region). The PL below 1290 meV originates from the confined states of the trap and is localized in space. In the case of the $L = 2 \mu\text{m}$ trap, the PL is also structured in energy, forming well-defined con-

finned modes. The PL consists of narrow lines, which correspond to quantum dot resonances. Spatially integrated spectra of traps with different L are summarized in Fig. SI 3e. As expected, the lowest confined energy blueshifts with decreasing L . For traps with $L < 5 \mu\text{m}$, individual confined modes can be identified.

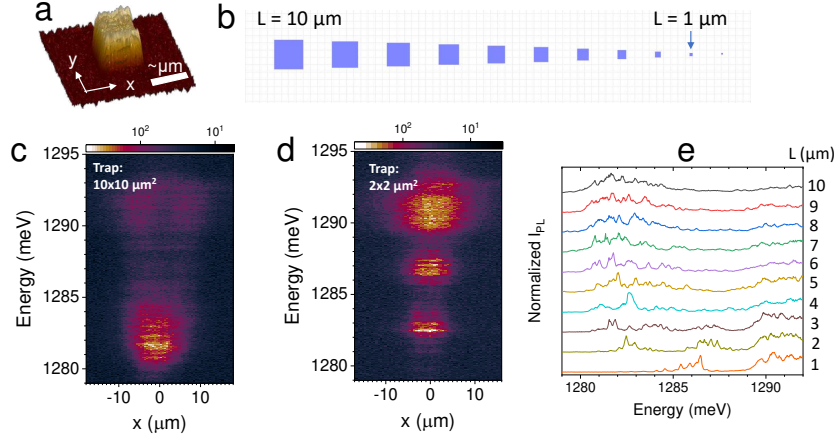


Fig. SI 3: **Photonic confinement.** **a** Exemplary AFM of a $L \times L = 4 \times 4 \mu\text{m}^2$ trap. The height of the mesa is $\approx 10 \text{ nm}$. **b** The size of the traps varies from $L = 10 \mu\text{m}$ down to $L = 1 \mu\text{m}$. **c,d** Spatially and spectrally resolved photoluminescence of non-resonantly excited $10 \times 10 \mu\text{m}^2$ and $2 \times 2 \mu\text{m}^2$ traps, respectively. The color bars represent the PL intensity in arbitrary units. **e** Spatially integrated spectra as a function of L .

4. Trap dispersion

Here, we discuss the angular distribution of the PL of QDs within traps (discussed in the section above). The measurements were done using a standard back focal plane imaging technique, which allows to obtain the angular distribution of the emitted light, see e.g., Ref. [4]. For MCs, this angle is directly related to the in-plane momentum of photons.

Figure SI 4a shows an angle-resolved PL of a $4 \times 4 \mu\text{m}^2$ trap. The emission with parabolic dispersion above 1306 meV originates from the spatially extended etched region of MC, where there is no lateral confinement. An angle-integrated spectrum is shown in Fig. SI 4b. It shows that the emission consists of overlapping spectrally narrow lines. Hence, we directly see that the emission of QDs is filtered by the parabolic dispersion of the cavity. Below 1306 meV, PL spectrum is quantized in energy, leading to the flat (dispersion-less) emission. From the dispersive part, we can determine the optical linewidth of about 0.9 meV for the zero in-plane momentum and, thus, the quality factor $Q_o \approx 1450$.

5. Trap PL excitation power dependence

At low optical excitation powers, the trap emission consists of spectrally narrow lines due to the QD resonances. Figure SI 5a shows a PL map of a $4 \times 4 \mu\text{m}^2$ trap as a function of the power of the non-resonant laser (P_{laser}). At the lowest power $P_{\text{laser}} = 60 \mu\text{W}$, the spectrum consists of narrow lines, cf. Fig. SI 5b. As the P_{laser} increases, the intensity increases and the lines broaden spectrally. The spectrum for the highest $P_{\text{laser}} = 0.64 \text{ mW}$ in Fig. SI 5c shows only the spectral envelopes given by the spectral width of the confined modes of the trap. Here, we use the spectral width of the PL under this condition as another way to determine the optical quality factor of the confined modes: $Q_o \approx 1600$, which is comparable to the one determined from the PL dispersion in the previous section.

We note that the PL of the photonic continuum (above 1293 meV) shows the typical saturation of the integrated PL as a function of P_{laser} , cf. black curve of Fig. SI 5d. However, the integrated PL of the individual confined levels shows a more complex behavior with a fast initial growth of the intensity, followed by a partial decrease and then becoming constant, as depicted by the colored curves of Fig. SI 5d. This behavior is currently under investigation.

6. Bulk acoustic resonators

Bulk acoustic wave resonators (BAR) were fabricated on the top of the MC sample using a procedure described in Ref. [5]. A BAR is schematically shown in Fig. SI 6a. It consists of a bottom Ti/Au (10/30 nm) contact, a layer of piezoelectric ZnO ($d_{\text{ZnO}} \approx 300 \text{ nm}$) and a top Ti/Al/Ti (10/30/10) contact. A BAR is an acoustic resonator. To a first approximation, its central frequency is $F_{\text{BAR}} \approx v_{\text{ZnO}} / (2d_{\text{ZnO}})$, where $v_{\text{ZnO}} = 6070 \text{ m/s}$ is the velocity of a longitudinal bulk acoustic wave (BAW). In reality, due to the mass-density of the contacts the frequency is lower. Since BAR is a low-Q acoustic resonator, it has a bandwidth of several GHz around F_{BAR} [5]. When a monochromatic microwave signal (RF) with a frequency F_{RF} around F_{BAR} is applied to the BAR, the latter generates a BAW of the same frequency (F_{RF}). Reciprocally, a BAR can convert BAWs into an RF signal.

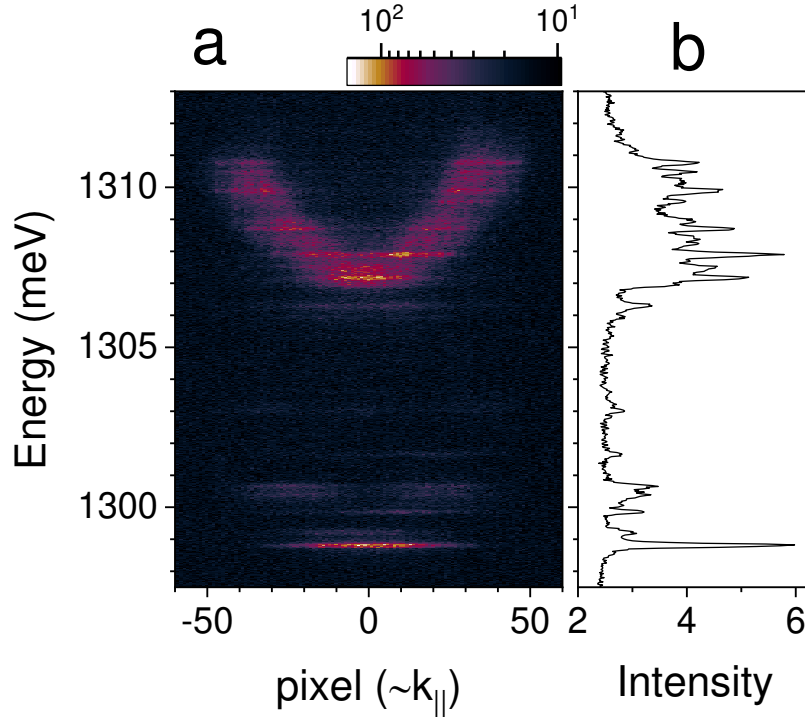


Fig. SI 4: **Angular dispersion of trap emission.** **a** Emission of $4 \times 4 \mu\text{m}^2$ trap resolved in energy and in-plane momentum, k_{\parallel} , prop. to the emission angle. The color bar represents the PL intensity in arbitrary units. **b** Spectrum integrated over k_{\parallel} . The intensity is expressed in arbitrary units.

This bi-directional conversion between RF and BAWs can be used to study the generation and propagation of GHz BAWs in complex structures such as MCs [6] using conventional microwave instruments, e.g. a vector network analyzer (VNA). In this method, VNA sweeps the frequency and measures the amplitude and the phase of the reflected RF signal corresponding to the s_{11} parameter. Since both the phase and the amplitude are available, one can obtain an effective time response of the signal via the inverse Fourier transform. This allows one to differentiate between the electromagnetic and acoustic contributions due to the huge difference in their propagation velocities.

Figure SI 6b shows a time-domain representation of the s_{11} of a BAR on a MC with quantum dots over the 3–10 GHz range recorded at 5 K. One can clearly see time-periodic peaks corresponding to the consecutive BAW echoes due to the multiple reflections at the bottom and the top sides of the sample. The time-separation between the adjacent echoes corresponding to the round trip time, is $\Delta T_{\text{rt}} = 2d_{\text{sample}}/v_{\text{ZnO}}$, where the total thickness of the sample is the sum of the MC and substrate thicknesses $d_{\text{sample}} = d_{\text{MC}} + d_{\text{subst.}}$. In the present case $d_{\text{subst.}} = 350 \pm 25 \mu\text{m}$.

Figure SI 6c shows the frequency components of the first echo (black curve) as well as of the first four echoes (red curve). This representation corresponds to an effective transmission measurement through the sample. We see that the response covers a broad range of frequencies from 3 GHz to above 10 GHz. The complex spectral shape of the curves originates from the fact that the MC acts as a filter for some acoustic frequencies. Overall, there is a correspondence between the experiment and the simulation of Fig. SI 1c. The region of small amplitudes between 5.5 GHz and 6 GHz is the acoustic stopband of the MC. There are two narrow peaks within the stopband. The one at about 5.6 GHz is likely the intended acoustic cavity mode. The other around 5.8 GHz is possibly the mode formed by the BAW and the upper mirror, as has already been observed in Ref. [6]. The interference of the acoustic echoes leads to formation of high-Q Fabry-Perot modes, cf. Fig. SI 6d. Finally, acoustic echoes propagate laterally, as is schematically shown in Fig. SI 6a by the solid green arrows, which allows us to use BARs with the apertures for the optical experiments [6].

7. Raw PL vs. A_{BAW} data and filtering procedure

Figure SI 7 shows a PL map of an as-measured QD spectrum in a trap as a function of the modulation amplitude. This data was post-processed to obtain Fig. 3b of the main text. A Wolfram Mathematica software was used to apply a bandpass filter to the image data was to remove low frequency PL components along the y-direction (energy axis). Specifically, low-frequency filter cut-off was set to 0.17, while the kern was set to 25.

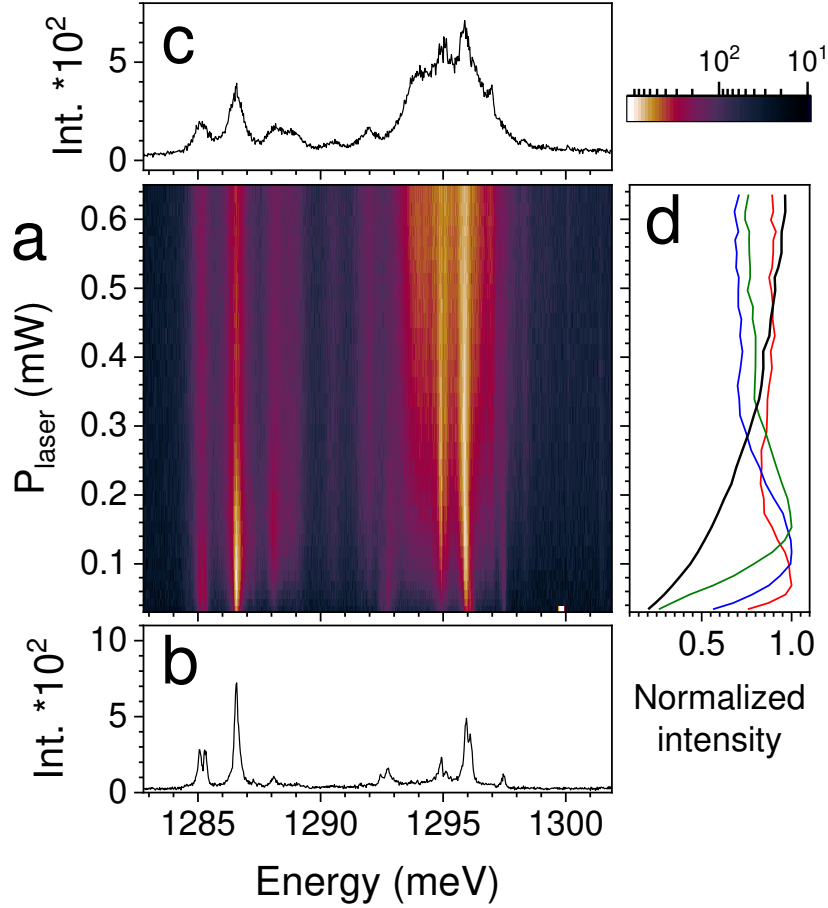


Fig. SI 5: **Emission of QDs in a trap vs. excitation power.** **a** Spatially integrated PL spectrum of a $4 \times 4 \mu\text{m}^2$ trap as a function of the non-resonant laser power (P_{laser}) at 5 K. The color bar represents the PL intensity in arbitrary units. Exemplary spectra for the lowest and the highest P_{laser} are shown **(b)** below and **(c)** above, respectively. The intensity is expressed in arbitrary units. **d** Energy-integrated normalized intensity profiles vs. P_{laser} for the ground state (red curve), first (blue curve) and second (green curve) excited state and the continuum (black curve).

Supplementary References

- [1] A. S. Kuznetsov, K. Biermann, A. A. Reynoso, A. Fainstein, and P. V. Santos, Microcavity phonoritons – a coherent optical-to-microwave interface, *Nat. Commun.* **14**, 5470 (2023).
- [2] A. Fainstein, N. D. Lanzillotti-Kimura, B. Jusserand, and B. Perrin, Strong optical-mechanical coupling in a vertical GaAs/AlAs microcavity for subterahertz phonons and near-infrared light, *Phys. Rev. Lett.* **110**, 037403 (2013).
- [3] P. Sesin, A. S. Kuznetsov, G. Rozas, S. Anguiano, A. E. Bruchhausen, A. Lemaître, K. Biermann, P. V. Santos, and A. Fainstein, Giant optomechanical coupling and dephasing protection with cavity exciton-polaritons, *Phys. Rev. Res.* **5**, L042035 (2023).
- [4] A. S. Kuznetsov, P. L. J. Helgers, K. Biermann, and P. V. Santos, Quantum confinement of exciton-polaritons in a structured (Al,Ga)As microcavity, *Phys. Rev. B* **97**, 195309 (2018).
- [5] D. H. O. Machado, A. Crespo-Poveda, A. S. Kuznetsov, K. Biermann, L. V. A. Scalvi, and P. V. Santos, Generation and propagation of super-high-frequency bulk acoustic wave in GaAs, *Phys. Rev. Appl.* **12**, 1 (2019).
- [6] A. S. Kuznetsov, D. H. O. Machado, K. Biermann, and P. V. Santos, Electrically Driven Microcavity Exciton-Polariton Optomechanics at 20 GHz, *Phys. Rev. X* **11**, 021020 (2021).

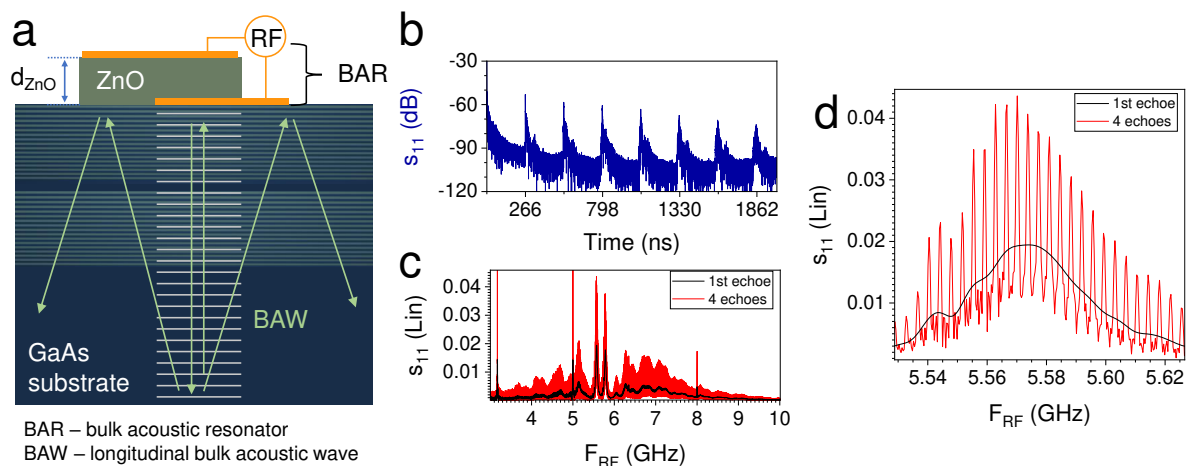


Fig. SI 6: **Bulk acoustic wave resonators (BAR).** **a** Sketch of a BAR on top of a planar MC. When driven by the radio frequency signal, BAR generates a bulk acoustic wave (BAW, horizontal thin lines). The BAW undergoes multiple reflections at the top and bottom surfaces (vertical arrows), with partial lateral propagation (tilted arrows). **b** Time-domain s_{11} response of a BAR in the 3–10 GHz range. Equidistant peaks correspond to BAW echoes at 5 K. **c** Time-gated s_{11} obtained for one and four echoes of the panel **b**. **d** An expanded range of the curves in **c** around the cavity mode.

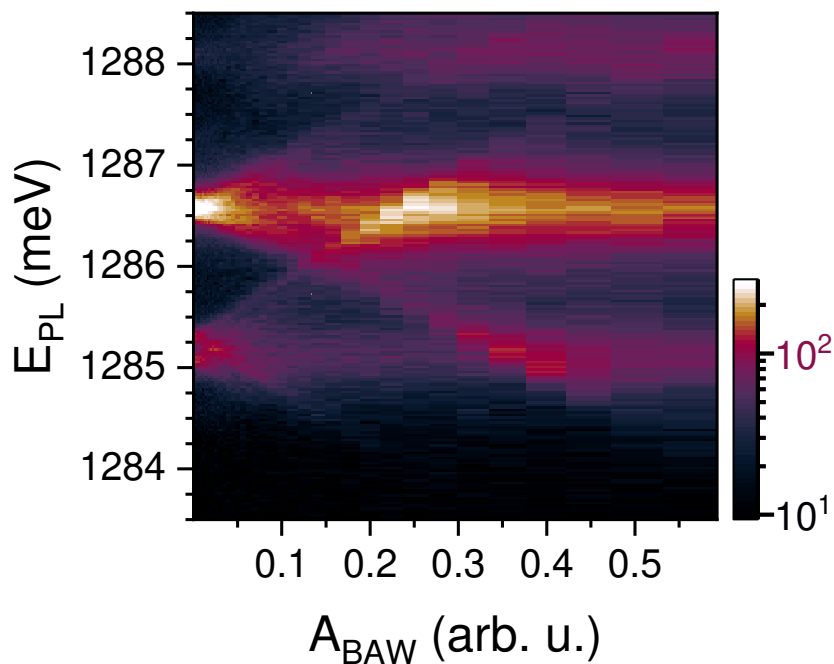


Fig. SI 7: **As-measured data.** A PL map with as-measured data, which was used to obtain a filtered image shown in the Fig. 3b of the main text. The color bar represents the PL intensity in arbitrary units.